

Microstructural heterogeneities governing the deformation of $\text{Cu}_{47.5}\text{Zr}_{47.5}\text{Al}_5$ bulk metallic glass composites

S. Pauly^{a,*}, G. Liu^b, G. Wang^a, U. Kühn^a, N. Mattern^a, J. Eckert^{a,c}

^aIFW Dresden, Institut für Komplexe Materialien, Helmholtzstraße 20, D-01069 Dresden, Germany

^bState Key Laboratory for Mechanical Behavior of Materials, School of Materials Science and Engineering, Xi'an Jiaotong University, Xi'an 710049, China

^cInstitut für Werkstoffwissenschaft, Technische Universität Dresden, D-01062 Dresden, Germany

Received 17 June 2009; accepted 24 July 2009

Available online 22 August 2009

Abstract

$\text{Cu}_{47.5}\text{Zr}_{47.5}\text{Al}_5$ rods with different volume fractions of crystalline B2 CuZr phase were prepared by copper mould casting. Based on microstructural investigations a solidification mechanism is proposed for these bulk metallic glass (BMG) composites. The composite microstructure enhances the compressive plasticity (plastic strain up to 14%) and both plastic strain as well as yield strength scale with the crystalline volume fraction. Yield strength and fracture strain were successfully calculated using a strength model, which considers percolation and an empirical three microstructural element body approach, respectively. Furthermore, B2 CuZr was synthesized by means of a thermal cycling treatment and uniaxial compression tests were carried out at room temperature. The intrinsic work-hardening caused by a martensitic transformation has strong implications on the deformation behaviour of the investigated $\text{Cu}_{47.5}\text{Zr}_{47.5}\text{Al}_5$ BMG composites.

© 2009 Acta Materialia Inc. Published by Elsevier Ltd. All rights reserved.

Keywords: Rapid solidification; Compression test; Bulk amorphous alloys; Shape memory alloys; Plastic deformation

1. Introduction

Glassy Cu–Zr ribbons have been investigated from the early 1980s onwards [1–3]. However, bulk metallic glass (BMG) formation in this binary system was only reported as late as 2004 [4–7]. Since then the Cu–Zr system has remained one of the rare binary bulk glass formers known to date [8,9]. In order to significantly improve the glass forming ability (GFA), third elements like Ti or Al can be added to the binary Cu–Zr alloys [10–14]. From an engineering point of view the binary and ternary Cu–Zr-based BMGs have a certain attractiveness as they exhibit considerable plastic strain along with high yield strength under room temperature compression. However, the plastic strain of Cu–Zr-based alloys critically depends on the actual com-

position of the alloy. It is pronounced in the vicinity of $\text{Cu}_{50}\text{Zr}_{50}$ and deteriorates if the composition is more Cu-rich [4,5,15,16]. Also, a significant plastic deformability has been reported for ternary $\text{Cu}_{47.5}\text{Zr}_{47.5}\text{Al}_5$ [17–19]. Because of this $\text{Cu}_{47.5}\text{Zr}_{47.5}\text{Al}_5$ was chosen for the current investigation.

It is well known that the introduction of a second phase can improve the deformation behaviour of BMGs [18,20–26]. Thereby the length scale, the distribution as well as the mechanical properties of the second phase, determine the properties of the partially crystalline BMGs (or BMG composites) [27]. This is essential to prevent catastrophic failure in these materials. When it comes to BMG composites in general Cu–Zr-based alloys are interesting in particular for another reason: crystalline CuZr can undergo a martensitic transformation (MT) from a cubic primitive B2 ($Pm\text{--}3m$) to a monoclinic B19' ($P2_1/m$ and Cm) phase, similarly to the NiTi system [28–30]. It has been suggested that this MT is responsible for the work hardening behav-

* Corresponding author.

E-mail address: s.pauly@ifw-dresden.de (S. Pauly).

our and the plasticity of this alloy family [23,31,32]. As the transformation from austenite (B2) to martensite (B1') is reversible, a shape memory effect (SME) arises in the CuZr alloy [29,33].

There are some reports about BMG composites of Cu–Zr–Al alloys and the phase which crystallizes first is B2 CuZr [21,23,24,32,34]. Thus, it is important to determine the mechanical properties of this phase and to understand its contribution to the deformation behaviour of BMG composites. To the best of the authors' knowledge the B2 CuZr phase has never been investigated before with respect to its elastic–plastic properties. This data will prove helpful for the systematic investigation of the influence of the crystalline phase on the mechanical properties of composites. Therefore, in the present work Cu_{47.5}Zr_{47.5}Al₅ rods were cast using different melting currents prior to solidification, a similar approach to Zhu et al. [35].

2. Experimental

Cu_{47.5}Zr_{47.5}Al₅ pre-alloys were synthesized by arc melting appropriate amounts of the constituting elements (purity $\geq 99.99\%$). The pre-alloyed ingots were re-melted at least four times in order to ensure chemical homogeneity. Approximately 5–8 g pieces of the ingots were used to produce 70 mm long rods with a diameter of 2 mm via suction casting into a water cooled copper mould. The temperature of the Cu_{47.5}Zr_{47.5}Al₅ melt was varied by applying different melting currents, namely 100, 130, 180 and 200 A, for approximately 20 s. As there was no possibility of measuring the temperature of the melt in the arc melter directly, we had to use this indirect method.

One rod was annealed for 16 h at 1073 K in an Ar atmosphere and then quenched to room temperature in an Ar flow within approximately 2 min. The rod was then thermally cycled in a Netzsch DIL 402C dilatometer between 193 and 673 K at a heating rate of 5 K min⁻¹.

Low temperature differential scanning calorimetry (DSC) was done in a Perkin–Elmer Diamond DSC with a heating rate of 20 K min⁻¹. Microstructural investigations were carried out with a Zeiss Axiophot optical microscope and a Hitachi TM1000 scanning electron microscope. Electron backscatter diffraction (EBSD) was performed in a Zeiss Gemini 1530 electron microscope equipped with an EBSD unit (Oxford). The specimens were characterized with a diffractometer (STOE STADI P) with MoK_{α1} radiation ($\lambda = 0.07093187$ nm) in transmission mode. Rietveld refinement of the diffraction patterns was conducted with the program “Fullprof”.

The elastic properties were determined with an Olympus Panametrics-NDT 5900PR ultrasonic testing device. For the compression tests an Instron 5869 was used with a constant strain rate of 1×10^{-4} s⁻¹. A laser-extensometer (Fiedler) monitored the strain directly on the sample.

3. Results and discussion

3.1. Microstructure and solidification mechanism

Fig. 1 displays the typical microstructure of an as cast Cu_{47.5}Zr_{47.5}Al₅ rod with a diameter of 2 mm. A dark precipitate with a diameter of 400–500 μm was embedded in a brighter, featureless matrix. In the centre of the precipitate a substructure is clearly visible, consisting of dendrites and a very fine eutectic mixture (inset in the lower left corner of Fig. 1). Towards the particle–matrix interface this substructure vanishes and can no longer be resolved by scanning electron microscopy (SEM). To identify the crystalline phase we performed EBSD measurements at the outer regions of the precipitate, as indicated in Fig. 1. The Kikuchi lines (inset in the upper right corner of Fig. 1) can all be indexed according to the B2 CuZr phase with a cubic primitive lattice ($Pm\bar{3}m$) and a lattice constant of $a = 0.326$ nm. In the bright matrix, however, no hint of crystallinity can be revealed by the EBSD measurements. This means that the dark–bright contrast that became obvious in BSE mode is a phase contrast between B2 CuZr and the glassy matrix. The presence of a glassy phase is, moreover, proved by DSC scans (not shown here), as well as by the broad scattering maximum found in the diffraction patterns (Fig. 3).

The observed microstructural features are common for Cu–Zr-based composites [14,21,24,34,36]. The second phase particles were spherical in most cases and sometimes impinged upon each other. Their diameters typically varied between 10 and 500 μm . Not just the size, but also the distribution of the precipitates was non-uniform. This was found at the surface, where the cooling rate was highest, as well as in the centre of the rods. In the larger precipitates a dendritic substructure can be seen that always disappears

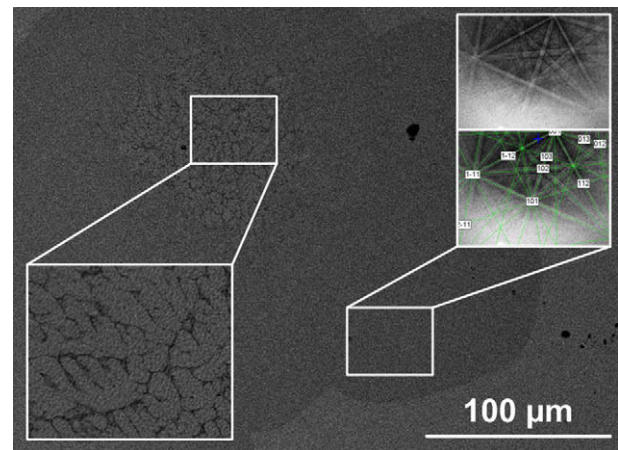


Fig. 1. Microstructure of an as cast Cu_{47.5}Zr_{47.5}Al₅ rod with a diameter of 2 mm. Within the dark precipitates a dendritic substructure can be revealed in some regions. EBSD patterns obtained from the featureless regions can be indexed according to the B2 CuZr phase. The sample was cast using a melting current of 200 A.

towards the interface with the glassy matrix. Interestingly, the average compositions of the crystals and the glass are identical within experimental error, namely $\text{Cu}_{47.5}\text{Zr}_{48.3}\text{Al}_{4.2}$. This matches well with the nominal composition of $\text{Cu}_{47.5}\text{Zr}_{47.5}\text{Al}_5$. At the same time this means that the contrast in BSE mode cannot be explained by compositional differences.

However, the primary dendrites have a distinct composition from the very fine surrounding eutectic mixture. The composition of the dendrites was determined to be $\text{Cu}_{46}\text{Zr}_{50}\text{Al}_4$, while the eutectic mixture was enriched in Al and had an average composition of $\text{Cu}_{50}\text{Zr}_{40}\text{Al}_{10}$. Yokoyama et al. have shown that $\text{Cu}_{50}\text{Zr}_{40}\text{Al}_{10}$ constitutes a ternary eutectic mixture in the Cu–Zr–Al system [37]. Based on this information we suggest the following solidification mechanism.

The origin of dendrite nucleation is difficult to clarify, but several hints point to the fact that in the present case homogeneous nucleation occurs. First of all, no impurities can be detected in the precipitates that could act as heterogeneous nuclei, as has been found, for instance, in a Zr–Al–Cu–Ni alloy [38]. Also, heterogeneous nucleation at the copper mould can be ruled out as the melt only crystallizes in some regions at the surface of the rod. Besides, the cooling rate is highest here, and if crystallization can be suppressed it should be close to the copper mould. A gradient microstructure, as observed by Sun et al. [23], was not found in any of the $\text{Cu}_{47.5}\text{Zr}_{47.5}\text{Al}_5$ rods. In the case of homogeneous nucleation the nuclei would be expected to be distributed randomly in the melt, as would the crystals, which precipitate from them.

A high critical cooling rate of $4 \times 10^4 \text{ K s}^{-1}$ has been determined experimentally for a $\text{Cu}_{56}\text{Zr}_{44}$ glass [39], indicating a high driving force for crystallization. For comparison, in bulk metallic glass forming systems the critical cooling rate typically ranges between 10^0 and 10^3 K s^{-1} [8]. Recent thermodynamic calculations [40,41] yielded a very broad range of critical cooling rates, from 10^3 to 10^{-4} K s^{-1} . The large differences might have their origin in the fact that the driving forces for crystallization and the critical cooling rates have been calculated for either CuZr_2 or $\text{Cu}_7\text{Zr}_{10}$ as the primary crystallizing phase, instead of B2 CuZr. Furthermore, homogeneous nucleation was proposed for the same alloy by Zhu et al. [35].

Once the nuclei have formed the cooling rate is insufficient to avoid the growth of some dendrites. Nevertheless, the heat extraction was high enough to prevent excessive growth and, with it, complete crystallization of the melt. It is important to mention that the B2 CuZr phase crystallizes polymorphically from the $\text{Cu}_{47.5}\text{Zr}_{47.5}\text{Al}_5$ melt. The relatively rapid heat extraction suppressed eutectoid decomposition of B2 CuZr into the low temperature equilibrium phases $\text{Cu}_{10}\text{Zr}_7$ and CuZr_2 . The solubility of Al in the B2 CuZr dendrites was limited to approximately 4 at.%, as ascertained by energy-dispersive X-ray analysis measurements. Excess Al was rejected into the surrounding melt, which eventually solidified eutectically. As the

temperature decreased during solidification the diffusion necessary for the crystallization process was slowed down. The primary dendrites became smaller until finally their features could no longer be revealed by means of SEM. The precipitates appeared featureless near the interface with the matrix. While the crystals at the edge of the specimen grew towards the centre of the rod – the same direction in which the glass solidified – the spherical crystals grew radially. This process is schematically shown in Fig. 2.

The micrographs of the samples used for the compression test were optically analysed in order to establish the volume fractions of the crystalline and glassy phases. This way one only obtains information about the degree of crystallinity from one surface of the rod. We are aware that these values should be interpreted with care. Still, they are believed to give satisfactory estimates of the real crystalline volume fraction of the whole rod. Especially as X-ray diffraction (see below) corroborated the values. The crystalline volume fractions of the differently solidified specimens are listed in Table 2. Obviously, there is no trend for the crystalline volume fraction to vary with melting current or, rather, with the temperature of the melt prior to casting. This is in contrast to Zhu et al. [35]. Even the maximum superheating at a current of 200 A did not result in fully glassy material. Possibly the temperature of the melt was in all cases (all currents) too high, so that the cooling rate was insufficient to bypass the crystalline “blip” in the CCT diagram. In the present investigation the microstructure rather depended on the local cooling rate.

The constituent phases of the $\text{Cu}_{47.5}\text{Zr}_{47.5}\text{Al}_5$ specimens were also investigated by means of X-ray diffraction. The results are depicted in Fig. 3. The specimen cast at a melting current of 100 A appeared to be fully glassy, while in the other samples crystalline reflections were superimposed on the broad amorphous scattering maxima. The Bragg peaks can be allocated to the B2 CuZr and the B19' CuZr

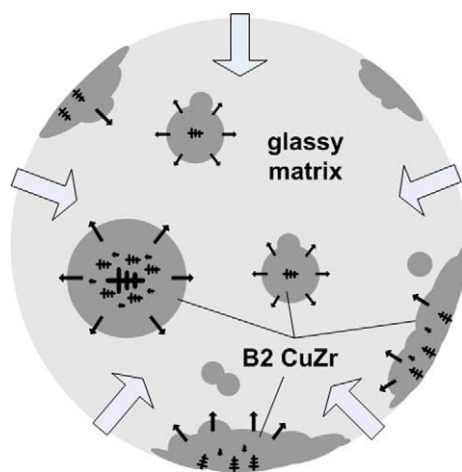


Fig. 2. Schematic illustration of the solidification mechanism of the $\text{Cu}_{47.5}\text{Zr}_{47.5}\text{Al}_5$ melt. While the melt solidified radially from the outside to the inside (large arrows), the B2 CuZr crystals grew radially at random positions, most likely because of homogeneous nucleation and differences in local cooling rate.

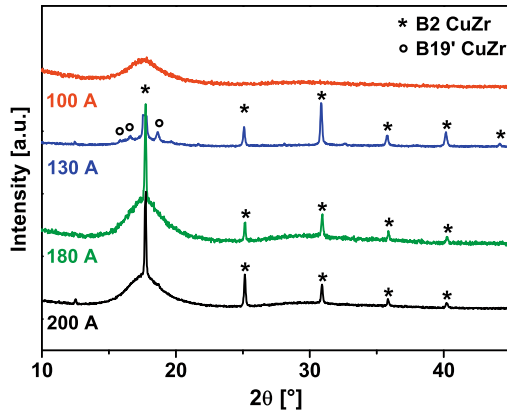


Fig. 3. X-ray diffraction pattern of $\text{Cu}_{47.5}\text{Zr}_{47.5}\text{Al}_5$ alloys melted with different currents in an arc melter for 20 s. Note that the strongest reflection of the sample cast with 130 A at $2\theta \approx 18^\circ$ has been cut off.

phases. Austenite (B2 CuZr) can transform into martensite (B19' CuZr) due to the stresses that occur during solidification, as well as plastic deformation at room temperature [32]. Clear B19' reflections were only found in the sample cast with a current of 130 A, which contained a high crystalline volume fraction (Table 2). Only part of the B2 phase was transformed and thus a substantial volume fraction of B2 CuZr had to be present in the sample to also detect the B19' phase [32]. Judging from the height of the crystalline peaks there should only be a small volume fraction of crystals present in the specimens cast with currents of 180 and 200 A. This confirms the crystalline volume fractions determined by means of optical analysis (Table 2).

We used the crystalline peaks to perform Rietveld refinement and treated the glassy scattering as background. Despite of the different solidification conditions, the lattice constant was found to be the same in all specimens. It scattered between 0.3262 and 0.3263 nm, which is close to the values reported for binary CuZr ($a = 0.3262$ nm) [29,42]. This implies that the incorporation of Al into the B2 CuZr phase does not affect the lattice constants.

3.2. SME of a $\text{Cu}_{47.5}\text{Zr}_{47.5}\text{Al}_5$ alloy

The B2 CuZr phase was only stable at temperatures above 988 K and decomposed into $\text{Cu}_{10}\text{Zr}_7$ and CuZr_2 if the system was given the time to equilibrate [43]. After quenching the alloy, which was annealed for 16 h at 1073 K, martensitic CuZr (B19' CuZr) was mainly formed (Fig. 4).

To obtain the B2 phase at room temperature the SME of the Cu–Zr-based alloys had to be exploited [29]. Fig. 5 shows the dilatation normalized with respect to the original sample length (dL/L_0) of a $\text{Cu}_{47.5}\text{Zr}_{47.5}\text{Al}_5$ rod which had been thermally cycled between 193 and 673 K. In the first heating step the martensite (B19') transformed to austenite (B2) at a temperature of ~ 473 K (A_s = austenite start temperature). The reverse martensitic transformation (MT) was associated with a negative volume effect. Upon cooling

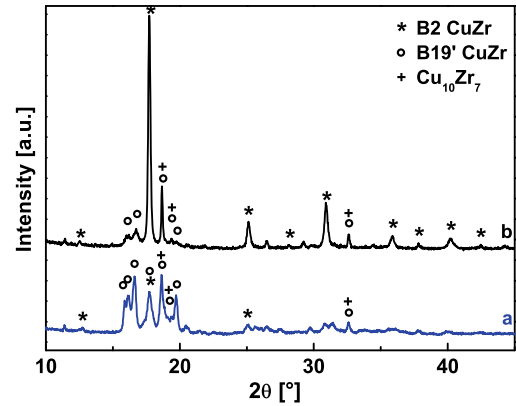


Fig. 4. XRD diffraction patterns of the rod, which was annealed at 800 °C for 16 h and then quenched to room temperature in ~ 2 min (a). This sample mainly consists of martensite (B19' CuZr). After thermal cycling between 193 and 673 K (b) austenite (B2 CuZr) can be stabilized, even at room temperature.

the sample transformed back to martensite at ~ 223 K (M_s = martensite start temperature) in the first cycle. The forward MT was linked to a positive volume effect, which is in accord with reports from other groups [29,42]. In the second thermal cycle A_s was shifted to higher temperatures and M_s was lowered. Consequently, the hysteresis increased, and this held true for up to at least six cycles. In the fifth cycle M_s was as low as 223 K. This means that austenite was stabilized to low temperatures. The crystalline samples treated that way were investigated by X-ray diffraction and the martensite had transformed into austenite (Fig. 4). The strongest reflections all stemmed from B2 CuZr, whereas the B19' CuZr Bragg peaks had decreased in intensity. Yet, one peak at around $2\theta = 18.6^\circ$ seemed to gain in intensity and sharpness. One cannot allocate it unambiguously to either B19' CuZr or $\text{Cu}_{10}\text{Zr}_7$, however,

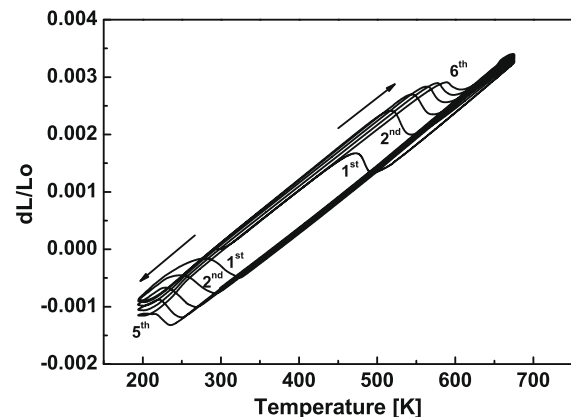


Fig. 5. Dilatometry of a $\text{Cu}_{47.5}\text{Zr}_{47.5}\text{Al}_5$ sample annealed for 16 h at 1073 K. With increasing cycle number A_s and M_s are shifted to higher and lower values, respectively. Upon heating the remaining martensite transformed to austenite, causing a negative dilatation. The austenite to martensite transformation is associated with a positive volume effect. The decrease in volume change points to the fact that the shape memory behaviour was not complete and some martensite did not transform to austenite upon heating.

the following reasons support the fact that a small volume fraction of $\text{Cu}_{10}\text{Zr}_7$ was present after thermal cycling. (i) All B19' reflections became weaker. Why should one become sharper and stronger? (ii) $\text{Cu}_{10}\text{Zr}_7$ is one of the equilibrium phases at temperatures below 988 K. Furthermore, it has been shown [44] that $\text{Cu}_{10}\text{Zr}_7$ precipitates prior to CuZr_2 , i.e. the second low temperature equilibrium phase in $\text{Cu}_{47.5}\text{Zr}_{47.5}\text{Al}_5$. Consequently, we expect that B2 CuZr partly decomposes eutectoidly into the low temperature equilibrium phases during thermal cycling.

However, it should be expected, at the same time, that some martensite remains in the alloy after heat treatment. Hysteresis of the dilatation behaviour indicates that the shape recovery of $\text{Cu}_{47.5}\text{Zr}_{47.5}\text{Al}_5$ is not complete – a small amount of martensite does not transform back to austenite. This is consistent with reports by Koval et al., which found a shape recovery of 85–90% in binary crystalline CuZr [29].

In the X-ray diffraction pattern (Fig. 6) Bragg reflections from all lattice planes were detected. It is a cubic primitive lattice ($Pm\bar{3}m$) with $a = 0.3264$ nm, which is only marginally larger than the lattice constants in the composites.

3.3. Mechanical properties

In the following we discuss how the microstructure and the different crystalline volume fractions affect the mechanical properties upon compressive deformation.

Prior to destruction of the specimens in the compression test device the elastic properties of the samples were investigated by ultrasonic sound velocity measurements. The data is summarized in Tables 1 and 2. The Young's modulus of the B2 CuZr phase (82 GPa) is slightly lower than that of the $\text{Cu}_{47.5}\text{Zr}_{47.5}\text{Al}_5$ glass (89 GPa). As a rule of thumb one usually assumes that the Young's moduli of BMGs are lower than those of their crystalline counterparts [8]. The Cu–Zr-based glasses are apparently an exception to this rule. Also, the Poisson ratio (ν), the shear (G) and the bulk modulus (B) show only small variations. In the case of the composites only the matrix contributes to the signal. As a result, the mechanical properties of the composites were identical, regardless of the number of crys-

tals (not shown here). Yet, when the crystalline volume fraction reached 50 vol.% the ultrasonic sound signal became too noisy to determine the elastic properties. The crystalline precipitates caused scattering of the signal, similarly to pores. Even though structurally completely different, the elastic properties of B2 CuZr in $\text{Cu}_{47.5}\text{Zr}_{47.5}\text{Al}_5$ and of the glassy phase were remarkably compatible. This might be a key factor for the enhancement of plasticity in Cu–Zr-based BMGs, as discussed below.

The compression test curves of several $\text{Cu}_{47.5}\text{Zr}_{47.5}\text{Al}_5$ rods cast using different melting currents are shown in Fig. 6. The characteristic deformation properties are summarized in Table 2. At first glance the investigated $\text{Cu}_{47.5}\text{Zr}_{47.5}\text{Al}_5$ specimens had a wide range of yield strengths (550–1670 MPa) and a significant variation in the fracture strain (3.1–14.9%). However, if one compares the data for samples with similar crystalline volume fractions the scattering decreases. The yield strength measured in different samples of the same rod (e.g. cast with a melting current of 180 A) was reproducible within a scattering width of ~ 100 MPa, which roughly corresponds to an error of 6%. A similar statement holds true for the fracture strain. Yet, the fracture strain seemed to be more sensitive to microstructural changes. A crystalline volume fraction around 10 vol.% could double the plastic strain compared with a composite containing only 1–5 vol.% B2 CuZr crystals. These results show how strongly the microstructure affects the deformation behaviour in Cu–Zr-based BMG composites. Possibly, some of the discrepancies in plasticity reported in this system [17,45] can be traced back to small amounts of crystals that have not been detected during the investigations. To demonstrate the influence of the microstructure, the yield strength is plotted as a function of the crystalline volume fraction in Fig. 8. When the crystalline volume fraction was between 0 and 5 vol.% the yield strength scattered around ~ 1600 MPa. A significant increase in the amount of B2 CuZr phase caused the yield strength to drop. At 50 vol.% crystals the yield strength reached a value of 550 MPa. This is close to the yield strength (450–490 MPa) of fully crystalline specimens. This general trend of a decreasing yield strength with increasing amount of crystalline phase is in accord with reports on similar Cu–Zr–Al alloys by other groups [23,46].

Fig. 9 shows the variation in fracture strain with crystalline volume fraction. Interestingly, small amounts of crystalline phase (5–10 vol.%) lead to an enhanced plasticity of between 6.7% and 8.1% (Table 2). The beneficial effect on plasticity continued up to a crystalline volume fraction of 30 vol.%. At higher crystalline contents B2 CuZr determined the deformation behaviour and plasticity decreased. In the fully crystalline sample it was around 8.8%. This is a high value for an intermetallic compound [47–49]. Obviously, there was an optimum crystalline volume fraction in $\text{Cu}_{47.5}\text{Zr}_{47.5}\text{Al}_5$ BMG composites causing maximum fracture strain (see Fig. 9).

The Young's moduli determined by compression tests were in agreement with the values obtained by ultrasonic

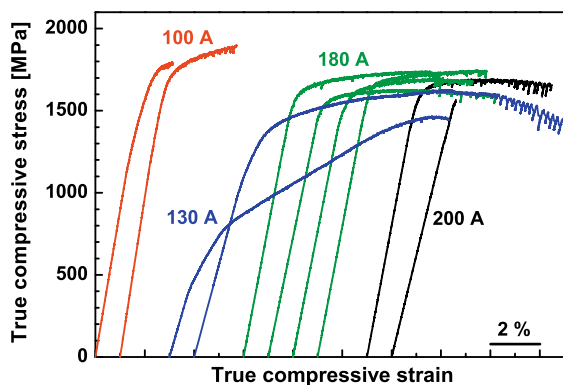


Fig. 6. Stress–strain curves for $\text{Cu}_{47.5}\text{Zr}_{47.5}\text{Al}_5$ rods cast using melting currents between 100 and 200 A for 20 s before solidification.

Table 1
Elastic properties as obtained from ultrasonic testing of B2 CuZr and the amorphous phase.

Phase	Young's modulus (GPa)	Poisson ratio	Shear modulus (GPa)	Bulk modulus (GPa)
B2 CuZr	82 ± 2	0.385 ± 0.004	29 ± 1	118 ± 3
Glass	89 ± 2	0.373 ± 0.003	33 ± 2	117 ± 3

The density, which is necessary for calculation of the elastic properties, was measured employing the Archimedean principle. The values are averaged over up to 10 independent measurements.

testing. Generally, the ultrasonic data were believed to be more precise. During compressive loading the elastic regime can sometimes be identified only with difficulty. Surfaces that are not perfectly flat and parallel can cause a curvature in the linear elastic part of the compression test curve. This causes a relatively larger error (see Table 2). The typical error in the determination of E is expected to be around ±15 GPa. The greatest deviation in Young's modulus was found in the sample cast with a melting current of 130 A. Probably improper loading conditions (slightly non-parallel end faces of the rods) in the early stages of the test caused the inaccurate determination of Young's modulus. As stated above, ultrasonic measurement failed for one of the two samples because of too high a crystalline volume fraction (50 vol.%), which reduced the signal strength so that it was lost in the noise. The second sample cast at a melting current of 200 A failed catastrophically, without any hint of plasticity. In the whole investigation it was the only specimen to show premature failure. Thus, we assume that this result was an artefact resulting from casting flaws or improper loading conditions.

Structural heterogeneities of different length scales have been found to be beneficial for plastic deformability [27]. Inoue et al. attributed the large plasticity of a Cu₅₀Zr₅₀ alloy to the coalescence of crystals having a diameter of ~5 nm in shear bands [20]. This mechanism was supposed

to cause deflection and branching of shear bands in the glassy matrix, resulting in a strain hardening effect [20]. Similarly, nano-scaled inhomogeneities (clusters as well as nanocrystals) have been reported to enhance plastic strain in a Cu_{47.5}Zr_{47.5}Al₅ BMG [17,50]. The heterogeneities acted as obstacles during shear band propagation due to local stress–strain differences, leaving a wavy shear band movement. The increase in surface also increases the dissipated energy of the shear band and, thereby, the plasticity [51]. At the same time micron scale B2 CuZr crystals increased the plastic deformability [23,46,52]. As the elastic properties of the glassy phase and the B2 CuZr crystals were nearly identical, no local stress concentrations should have arisen at the glass–crystal interface during compressive loading. When a shear band is generated and propagates through the specimen it will eventually reach a B2 CuZr crystal. This phase is quite ductile (see Fig. 7) and can accommodate the strain. Furthermore, the crystalline regions that have been deformed undergo a martensitic transformation [32] and, subsequently, become harder than the undeformed regions. It is more than likely that the undeformed regions will accommodate further strain, causing work hardening and preventing premature failure of the composite. In this way the unhindered, catastrophic propagation of shear bands is prevented. In a crystalline Ti₅₀Cu₅₀ alloy the martensitic regions have been found to

Table 2
Elastic–plastic properties of differently solidified Cu_{47.5}Zr_{47.5}Al₅.

Melting current (A)	No.	Young's modulus (GPa)		Yield strength (MPa)	Maximum stress (MPa)	Fracture strain (%)	Crystal volume fraction (%)
		CT	UT				
100	1	89 ± 15	90 ± 2	1540 ± 50	1800 ± 10	3.1 ± 1	1 + 5
	2	97 ± 15	88 ± 2	1670 ± 50	1900 ± 10	4.7 ± 1	5 ± 5
130	1	52 ± 20	n.a.	550 ± 50	1470 ± 10	11.3 ± 1	50 ± 5
	2	70 ± 20	89 ± 2	1250 ± 50	1630 ± 10	14.9 ± 1	30 ± 5
180	1	79 ± 15	88 ± 2	1600 ± 50	1740 ± 10	8.1 ± 1	10 ± 5
	2	72 ± 15	88 ± 2	1550 ± 50	1630 ± 10	5.0 ± 1	5 ± 5
	3	76 ± 15	89 ± 2	1550 ± 50	1700 ± 10	7.3 ± 1	n.a.
	4	79 ± 15	89 ± 2	1650 ± 50	1750 ± 10	6.8 ± 1	n.a.
200	1	80 ± 15	88 ± 2	1600 ± 50	1700 ± 10	7.5 ± 1	5 ± 5
	2	72 ± 15	89 ± 2	1480 ± 50	1680 ± 10	6.7 ± 1	10 ± 5
B2 CuZr	1	83 ± 15	81 ± 2	490 ± 30	2120 ± 10	8.7 ± 1	100
	2	79 ± 15	81 ± 2	450 ± 30	2060 ± 10	8.8 ± 1	100

CT, compression test.

UT, ultrasonic measurements.

The melting current was applied for ca. 20 s prior to solidification. A 0.2% offset yield strength was determined. For comparison Young's moduli determined by both CT and UT are given.

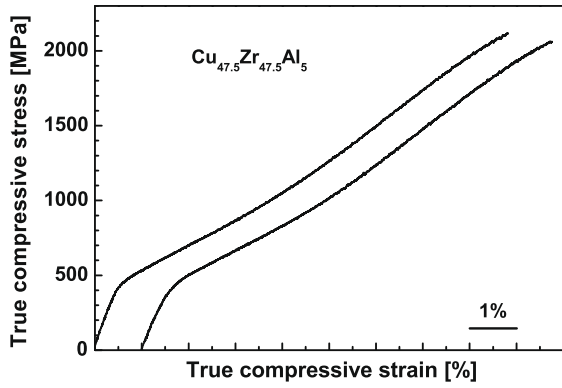


Fig. 7. Stress–strain curve for the $\text{Cu}_{47.5}\text{Zr}_{47.5}\text{Al}_5$ alloys, which were thermally cycled in order to obtain the B2 CuZr phase. The low yield stress as well as the TRIP-like work hardening are remarkable.

interrupt shear band propagation and avoid shear localization because of microcrack generation [53].

From Figs. 8 and 9 it can be deduced that $\text{Cu}_{47.5}\text{Zr}_{47.5}\text{Al}_5$ BMG composites with a B2 CuZr volume fraction between 5 and 10 vol.% combine both high strength and significant plasticity. Therefore, they basically inherit the desired properties from the glassy and the crystalline phases.

3.4. Modelling of the mechanical properties

Next to the experimental yield strengths measured for the different $\text{Cu}_{47.5}\text{Zr}_{47.5}\text{Al}_5$ composites, Fig. 8 depicts the calculated yield strengths using the rule of mixtures (ROM) and the load bearing model (dashed and dash-dotted lines). If the crystalline volume fraction is below 30 vol.% the yield strength of the composites can be described by the rule of mixtures. The glassy $\text{Cu}_{47.5}\text{Zr}_{47.5}\text{Al}_5$ matrix has a much higher yield strength than the B2 phase, the yield of the whole composite being controlled by the yield strength of the glass:

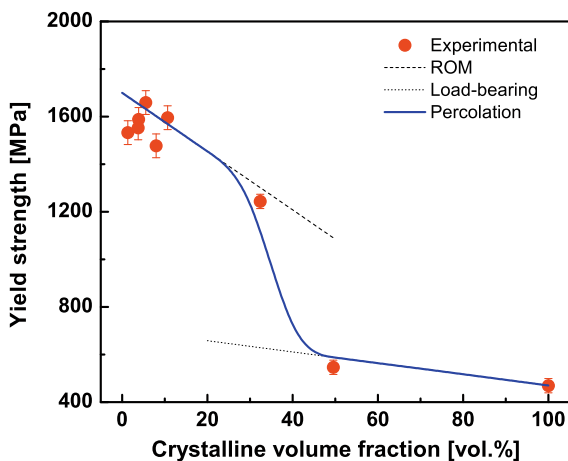


Fig. 8. Yield strengths of the different $\text{Cu}_{47.5}\text{Zr}_{47.5}\text{Al}_5$ rods as a function of the crystalline volume fraction. The yield strength decreased quickly with an increase in the crystalline volume fraction.

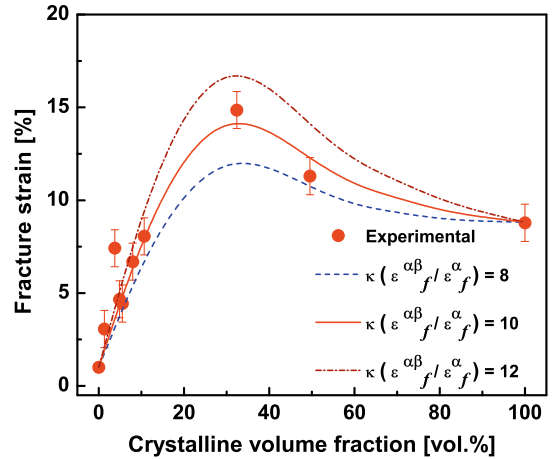


Fig. 9. Fracture strains of the different $\text{Cu}_{47.5}\text{Zr}_{47.5}\text{Al}_5$ rods as a function of the crystalline volume fraction. The fracture strain increased with an increase in the crystalline volume fraction. The dashed line is a guide for the eye.

$$\sigma^c = f_\alpha \sigma^\alpha + f_\beta \sigma^\beta, \tag{1}$$

where f and σ are the volume fraction and yield strength of the constituent phases and subscript/superscript α and β refer to the B2 CuZr phase and BMG phase, respectively. When the volume fraction of the B2 CuZr phase exceeds 50 vol.% the composite can be thought of as a crystalline matrix reinforced with a relatively harder glassy phase. Thus, as common in metal matrix composites, the yield strength can be obtained from the load bearing model [54,55]:

$$\sigma^c = \sigma^\alpha (1 + 0.5 f_\beta). \tag{2}$$

However, at crystalline volume fractions between 30 and 50 vol.% there is an obvious drop in the yield strength and a transition from the rule of mixtures to the load bearing model. This transition can be ascribed to a change in the microstructure. Fig. 10 shows the microstructures of $\text{Cu}_{47.5}\text{Zr}_{47.5}\text{Al}_5$ BMG matrix composites with crystalline volume fractions of 5, 30 and 50 vol.%. In the first case the B2 CuZr crystals are few and well separated. At 30 vol.% spherical crystals begin to impinge upon each other. This interpenetration continues with increasing numbers of crystals and at 50 vol.% the crystals form a structural framework. This microstructural transition can be linked to a critical volume fraction (v_{crit}) which has a

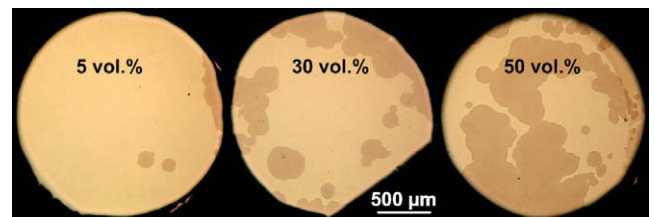


Fig. 10. $\text{Cu}_{47.5}\text{Zr}_{47.5}\text{Al}_5$ BMG matrix composites with different crystalline volume fractions. Between 30 and 50 vol.% the critical volume fraction was reached at which crystals interconnected and formed a structural framework.

physical meaning similar to the percolation threshold used to quantify the formation of long-range connectivity in random systems [56]. In two phase composites the percolation threshold generally has a value between 10 and 50 vol.%, depending on the morphology and size of the second phase and on the size ratio of the constituent phases [57]. In the present composites, where the precipitated B2 CuZr crystals had a typical size of several hundred micrometers and a spherical morphology within the centre of the composites, the critical crystalline volume fraction for the microstructural transition was determined to lie between 30 and 50 vol.%. This value is in good agreement with that (~ 35 vol.%) recently observed in Zr-based metallic glass matrix composites containing micrometer sized crystalline second phase precipitates [58]. The calculated curve, taking percolation into account (Fig. 8), agrees with the experimental data reasonably well.

In order to model the fracture strain of the composites we applied a model originally developed by Fan and Miodownik for a composite consisting of two ductile phases [59]. In this approach the composite is topologically transformed into a three microstructural element body (3-ebody). This is schematically shown in Fig. 11: element α represents B2 CuZr and element β the $\text{Cu}_{47.5}\text{Zr}_{47.5}\text{Al}_5$ BMG. The element $\alpha + \beta$ contains both B2 CuZr phase and $\text{Cu}_{47.5}\text{Zr}_{47.5}\text{Al}_5$ BMG in equal parts. The two phases are homogeneously partitioned with each other and form an ideal interdispersed structure. The fracture strain (ε_f^c) of the composites can be then described by the equation:

$$\varepsilon_f^c = f_{\alpha c} \varepsilon_f^\alpha + f_{\beta c} \varepsilon_f^\beta + \kappa f_{\alpha\beta} \varepsilon_f^{\alpha\beta}, \quad (3)$$

where $f_{\alpha c}$, $f_{\beta c}$ and $f_{\alpha\beta}$ are the volume fractions of the elements α , β and $\alpha + \beta$ and ε_f^α , ε_f^β , and $\varepsilon_f^{\alpha\beta}$ are the fracture strains of the α , β phases and the homogeneous $\alpha + \beta$ composite, respectively. κ is a dimensionless constant that is used to account for the constraint effect of the elements α and/or β on the element $\alpha + \beta$ [60]. All isolated B2 CuZr phases or coalesced B2 CuZr regions that had a size larger than $250 \mu\text{m}$ were classified as element α , and the remaining B2 CuZr phases as element $\alpha + \beta$ in the present case. This means that $f_\alpha = f_{\alpha c} + 1/2f_{\alpha\beta}$ and $f_\beta = f_{\beta c} + 1/2f_{\alpha\beta}$. Fig. 12 shows the evolution of $f_{\alpha c}$, $f_{\beta c}$ and $f_{\alpha\beta}$ with crystalline volume fraction. $f_{\alpha\beta}$ was found to increase initially with the crystalline volume fraction and to subsequently decrease after reaching a peak value at 30 vol.% crystals.

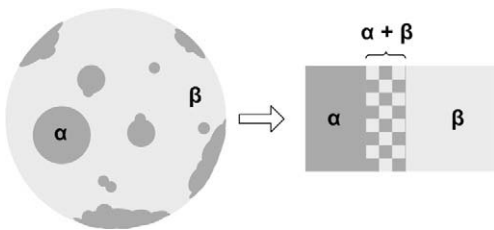


Fig. 11. Schematic illustration of the transformation from microstructure to the three microstructural element body. α Represents the B2 phase, β the BMG matrix and element $\beta + \alpha$ the B2 CuZr and glassy phases in equal amounts, assumed to form an ideal interdispersed structure.

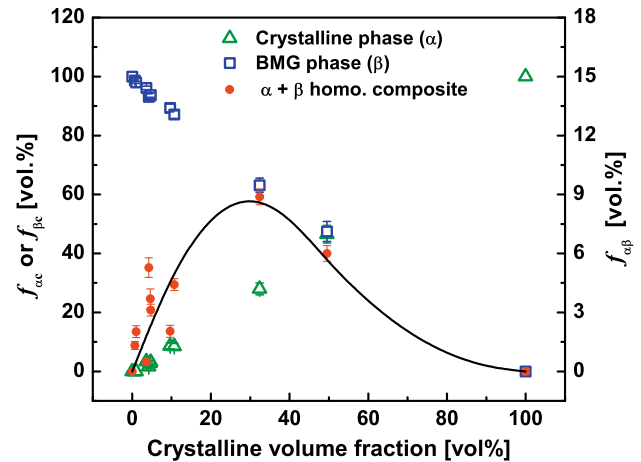


Fig. 12. Calculated volume fractions of element α (B2 CuZr), $f_{\alpha c}$, element β (BMG), $f_{\beta c}$ and element $\alpha + \beta$ (see text for explanation), $f_{\alpha\beta}$, as a function of the overall crystalline volume fraction.

Because element $\alpha + \beta$ had a ductility superior to both elements α and β a peak value was also reached for fracture strain at 30 vol.% crystals. Based on these considerations, the fracture strain of the composites was calculated using Eq. (3). The calculations are in good agreement with the experimental results (Fig. 10).

Although the specific deformation of BMGs is hard to model, the empirical approach used in the present paper successfully describes the fracture strain of BMG composites containing a relatively ductile second phase. In this process a good match of the elastic constants is essential. Furthermore, the calibrated high fracture strain for element $\alpha + \beta$ from modelling ($\kappa(\varepsilon_f^{\alpha\beta}/\varepsilon_f^\alpha) \approx 10$, Fig. 10) indicates that this homogeneously interdispersed microstructure should result in significantly improved ductility for the present composites, which could be helpful for microstructure design in developing advanced composites.

4. Conclusions

Cu–Zr-based BMG composites show a unique microstructure consisting of spherical B2 CuZr crystals embedded in a glassy matrix. The size and the distribution of the precipitates are heterogeneous and are apparently not influenced by the gradient in cooling rate inherent in the casting process. It is suggested that homogeneous nucleation and dendritic growth of the nuclei leads to the observed microstructure. The growth of crystals takes place coevally with glassy solidification of the melt from the outside to the inside of the rod. The mechanical properties of the B2 CuZr phase in $\text{Cu}_{47.5}\text{Zr}_{47.5}\text{Al}_5$ have been tested at room temperature for the first time. They are characterized by a low yield strength (450–490 MPa) and pronounced work hardening ($\sigma_{\text{max}} \approx 2000$ MPa), indicative of a transformation induced plasticity (TRIP) effect. Furthermore, the elastic properties of glassy Cu–Zr-based alloys and B2 CuZr show remarkable compatibility. This could explain the enhancement of plasticity without signif-

icant loss of strength at low crystalline volume fractions. This investigation has clearly demonstrated that the formation of in situ BMG composites in Cu–Zr-based alloys could solve the problem of limited ductility intrinsic to monolithic BMGs. The B2 CuZr phase showed significant work hardening behaviour. This, in turn, could possibly avoid necking of Cu–Zr-based BMG composites and thus even show ductility under tensile loading [61].

However, the distribution and the volume fraction of the crystalline phase are clearly difficult to control. More research is necessary to successfully tackle this problem.

Acknowledgments

The authors thank B. Bartusch, S. Donath, M. Frey and H. Schulze for technical assistance, and J. Das, H. Ehrenberg, K. S. Lee, K. Nikolowski, S. Scudino, M. Stoica, S. Venkataraman and H. Wendrock for stimulating discussions. Financial support provided by the European Union within the framework of the research and training network on Ductile BMG Composites (MRTN-CT-2003-504692) and through the Global Research Laboratory Program of the Korean Ministry of Education, Science and Technology is gratefully acknowledged. S.P. furthermore acknowledges financial support granted by the program “Promotions-förderung des Cusanuswerks”.

References

- [1] Buschow KHJ. *J Appl Phys* 1981;52:3319.
- [2] Altounian Z, Tu GH, Strøm-Olsen JO. *J Appl Phys* 1982;53:4755.
- [3] Inoue A, Masumoto T, Yano N. *J Mater Sci* 1984;19:3786.
- [4] Inoue A, Zhang W. *Mater Trans* 2004;45:584.
- [5] Xu D, Lohwongwatana B, Duan G, Johnson WL, Garland C. *Acta Mater* 2004;52:2621.
- [6] Tang MB, Zhao DQ, Pan MX, Wang WH. *Chin Phys Lett* 2004;21:901.
- [7] Wang WH, Lewandowski JJ, Greer AL. *J Mater Res* 2005;20:2307.
- [8] Inoue A. *Acta Mater* 2000;48:279.
- [9] Inoue A. *Proc Jpn Acad* 2005;81:156.
- [10] Inoue A, Zhang W, Zhang T, Kurosaka K. *Acta Mater* 2001;49:2645.
- [11] Inoue A, Zhang W, Zhang T, Kurosaka K. *Mater Trans* 2001;42:1149.
- [12] Xing LQ, Ochin P, Bigot J. *J Non-Cryst Solids* 1996;205:637.
- [13] Inoue A, Zhang W. *Mater Trans* 2002;43:2921.
- [14] Wang D, Tan H, Li Y. *Acta Mater* 2005;53:2969.
- [15] Zhu ZW, Zhang HF, Sun WS, Ding BZ, Hu ZQ. *Scripta Mater* 2006;54:1145.
- [16] Kwon OJ, Lee YK, Park SO, Lee JC, Kim YC, Fleury E. *Mater Sci Eng A* 2007;449:169.
- [17] Das J, Tang MB, Kim KB, Theissmann R, Baier F, Wang WH, et al. *Phys Rev Lett* 2005;94:205501.
- [18] Kim KB, Das J, Baier F, Tang MB, Wang WH, Eckert J. *Appl Phys Lett* 2006;88:051911.
- [19] Kumar G, Ohkubo T, Mukai T, Hono K. *Scripta Mater* 2007;57:173.
- [20] Inoue A, Zhang W, Tsurui T, Yavari AR, Greer AL. *Phil Mag Lett* 2005;85:221.
- [21] Pauly S, Das J, Duhamel C, Eckert J. *Adv Eng Mater* 2007;9:487.
- [22] Nagahama D, Ohkubo T, Mukai T, Hono K. *Mater Trans* 2005;46:1264.
- [23] Sun YF, Wei BC, Wang YR, Li WH, Cheung TL, Shek CH. *Appl Phys Lett* 2005;87:051905.
- [24] Das J, Pauly S, Duhamel C, Wei BC, Eckert J. *J Mater Res* 2007;22:326.
- [25] Pauly S, Das J, Duhamel C, Eckert J. *Metall Mater Trans A* 2007;39:1868.
- [26] Zhang QS, Zhang W, Xie GQ, Nakayama KS, Kimura H, Inoue A. *J Alloys Compd* 2007;431:236.
- [27] Eckert J, Das J, Pauly S, Duhamel C. *J Mater Res* 2007;22:285.
- [28] Carvalho EM, Harris IR. *J Mater Sci* 1980;15:1224.
- [29] Koval YN, Firstov GS, Kotko AV. *Scripta Metall Mater* 1992;27:1611.
- [30] Firstov GS, Van Humbeeck J, Koval YN. *J Phys IV* 2001;11:481.
- [31] Das J, Kim KB, Xu W, Wei BC, Zhang ZF, Wang WH, et al. *Mater Trans* 2006;47:2606.
- [32] Pauly S, Das J, Mattern JB, Kim N, Kim KB, Eckert DH. *J Scripta Mater* 2009;60:431.
- [33] Koval YN, Firstov GS, Delaey L, Humbeeck JV. *Scripta Metall Mater* 1994;31:799.
- [34] Jiang F, Zhang DH, Zhang LC, Zhang ZB, He L, Sun J, et al. *Mater Sci Eng A* 2007;467:139.
- [35] Zhu ZW, Zheng SJ, Zhang HF, Ding BZ, Hu ZQ, Liaw PK, et al. *J Mater Res* 2008;23:941.
- [36] Das J, Pauly S, Boström M, Durst K, Göken M, Eckert J. *J Alloys Compd* 2008. doi:10.1016/j.jallcom.2008.08.13.
- [37] Yokoyama Y, Inoue H, Fukaura K, Inoue A. *Mater Trans* 2002;43:575.
- [38] Gebert A, Eckert J, Schultz L. *Acta Mater* 1998;46:5475.
- [39] Gillessen F, Herlach DM. *Mater Sci Eng* 1988;97:147.
- [40] Abe T, Shimono M, Ode M, Onodera H. *Acta Mater* 2006;54:909.
- [41] Ge L, Hui X, Wang ER, Chen GL, Arroyave R, Liu ZK. *Intermetallics* 2008;16:27.
- [42] Zhalko-Titarenko AV, Yevlashina ML, Antonov VN, Yavorskii BY, Koval YN, Firstov GS. *Phys Stat Sol B* 1994;184:121.
- [43] Zeng KJ, Hämmäläinen M, Lukas HL. *J Phase Equilib* 1994;15:577.
- [44] Pauly S, Das J, Mattern N, Kim DH, Eckert J. *Intermetallics* 2009;17:453.
- [45] Cao QP, Li JF, Zhou YH, Jiang JZ. *Scripta Mater* 2008;59:673.
- [46] Jiang F, Zhang ZB, He L, Sun J. *J Mater Res* 2006;21:2638.
- [47] Izumi O. *Mater Trans* 1989;30:627.
- [48] Varin RA, Winnicka MB. *Mater Sci Eng A* 1990;137:93.
- [49] Liu CT, Stiegler JO. *Science* 1984;226:636.
- [50] Kim KB, Das J, Baier F, Tang MB, Wang WH. *Appl Phys Lett* 2006;88:051911.
- [51] Kim KB, Das J, Lee MH, Yi S, Fleury E, Zhang ZF, et al. *J Mater Res* 2008;23:6.
- [52] Qiu F, Shen P, Jiang ZG, Liu T, Jiang QC. *Appl Phys Lett* 2008;92:151912.
- [53] Kim KB, Song KA, Zhang XF, Yi S. *Appl Phys Lett* 2008;92:241915.
- [54] Nardone VC, Prewo KM. *Scripta Metall* 1986;20:43.
- [55] Zhang Q, Chen DL. *Scripta Mater* 2004;51:863.
- [56] Stauffer D, Aharony A. *Introduction to percolation theory*. London: Taylor & Francis; 1992.
- [57] Nan CW. *Prog Mater Sci* 1993;37:1.
- [58] Fu XL, Li Y, Schuh CA. *Scripta Mater* 2007;56:617.
- [59] Fan Z, Miodownik AP. *Scripta Metall Mater* 1993;28:895.
- [60] Liu G, Sun J, Nan CW, Chen KH. *Acta Mater* 2005;53:3459.
- [61] Ma E. *Scripta Mater* 2003;49:663.